Chinese Chemical Letters 34 (2023) 107787

Contents lists available at ScienceDirect

Chinese Chemical Letters

journal homepage: www.elsevier.com/locate/cclet

The introduction of cobalt element into nickel-organic framework for enhanced supercapacitive performance

Xinxin Hang*, Rui Yang, Yadan Xue, Shasha Zheng, Yuying Shan, Meng Du, Jiawei Zhao, Huan Pang*

School of Chemistry and Chemical Engineering and Institute for Innovative Materials and Energy, Yangzhou University, Yangzhou 225009, China

ARTICLE INFO

Article history:
Received 6 June 2022
Revised 27 June 2022
Accepted 24 August 2022
Available online 28 August 2022

Keywords:
Metal-organic frameworks
Bimetallic
Cobalt-nickel synergistic effect
Micro/nanostructures
Supercapacitors

ABSTRACT

Metal-organic frameworks (MOFs) as promising electrodes for supercapacitors are attracting increasing research interest. Herein, we report an effective strategy to improve the electrochemical performance of Ni-MOF for supercapacitor by introducing a secondary Co ion. The Co substitution of Ni in Ni-MOF can improve the intrinsic reactivity and stability. As a result, the bimetallic Co/Ni-MOF-1:15 with an optimal Co/Ni ratio delivers high specific capacitance (359 F/g at 0.5 A/g), good rate performance (81.5% retention at 5 A/g) and cycling stability (81% retention after 5000 cycles). These results demonstrate that the bimetallic synergistic strategy is an effective way to improve the pseudocapacitive performance of MOFs.

Metal-organic frameworks (MOFs) [1,2] have received increasing research interest in terms of their well-defined structures and potential applications in many fields [3], including catalysis [4–6], gas storage and separation [7,8], and water treatment [9]. Recently, MOFs are emerging as potential electrode materials for supercapacitors because their porosity provide the accommodation space for electrolyte, and valence changes of metal ions enable redox reaction with high theoretical capacity [10–15]. However, the intrinsic electrical insulation and structural instability of most MOFs limits their applications in electrochemical reactions, leading to low specific capacitance and cycling stability [16,17]. Incorporating another metal ion into MOFs is an effective strategy to solve this problem [18–23]. Generally, the interactions between different metal sites can modulate the electronic properties, facilitating to improve the electrical conductivity and generate more redox active sites. For example, Gao *et al.* have reported a bimetallic Ni/Co-MOF with dandelion-like structure that exhibits high specific capacitance of 758 F/g at 1 A/g, excellent rate performance and cycling stability benefitting from the unique structure and improved conductivity caused by the synergistic effect of Ni^{2+} and Co^{2+} [20]. Yang *et al.* have synthesized a layered Zn-doped Ni-MOF, which shows superior capacitance of 1620 and 854 F/g at 0.25 and 10 A/g, respectively, along with excellent cycling stability [22].

Ni-MOFs exhibit potential electrochemical properties and have been widely used as electrodes for supercapacitors [24–27]. In general, Ni-MOFs can deliver high specific capacitance but show poor rate performance and cycling stability that may be due to their structural instability during the fast charge-discharge process. Introducing a secondary metal ion to Ni-MOFs can facilitate the faradic redox reactions and improve the electrical conductivity and stability, thus achieving enhanced electrochemical performance [20–23].

Herein, we report a feasible approach for enhancing the electrochemical performance and stability of Ni-MOF by introducing a secondary Co element. Using Co/Ni-MOF-1:15 (1:15 represents the molar ratio of the initial material Co^{2+} and Ni^{2+}) as a demonstration, the introduction of Co^{2+}into Ni-MOF doesn't change the original crystal structure and morphology, but can improve the intrinsic reactivity and stability. In comparison with the Ni-MOF and Co-MOF, the bimetallic Co/Ni-MOF-1:15 exhibits higher specific capacitance of 359 F/g at 0.5 A/g along with better rate performance and cyclability owing to the synergistic effect between the optimal ratio of Co^{2+} and Ni^{2+}.

As shown in Fig. 1a, Ni-MOF, Co/Ni-MOF-x:y (x:y represents the molar ratio of the initial materials $Co(NO_3)_2{\cdot}6H_2O$ and $Ni(NO_3)_2{\cdot}6H_2O$; x:y = 1:15, 1:5 and 1:1), and Co-MOF were synthesized separately from a one-pot solvothermal reaction in dimethylformamide (DMF) solution containing metal salts and isonicotinic acid (4-Pyc), affording solid powder of different colors. Powder X-ray diffraction (PXRD) patterns (Fig. 2a) of the as-synthesized Ni-MOF, Co/Ni-MOF-x:y and Co-MOF are well matched with the

* Corresponding authors.
E-mail addresses: hangxinxin@yzu.edu.cn (X. Hang), panghuan@yzu.edu.cn, huanpangchem@hotmail.com (H. Pang).

https://doi.org/10.1016/j.cclet.2022.107787
1001-8417/

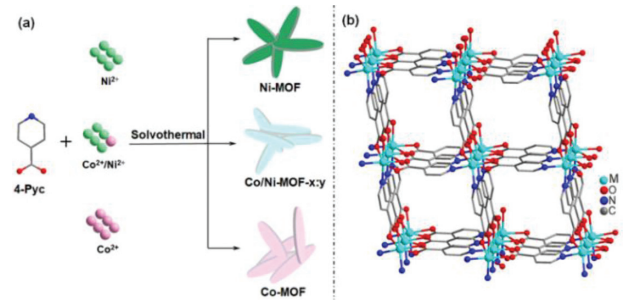

Fig. 1. (a) Schematic illustration of the synthesis procedure for Ni-MOF, Co/Ni-MOF-x:y and Co-MOF. (b) The crystal structure of the as-synthesized MOFs.

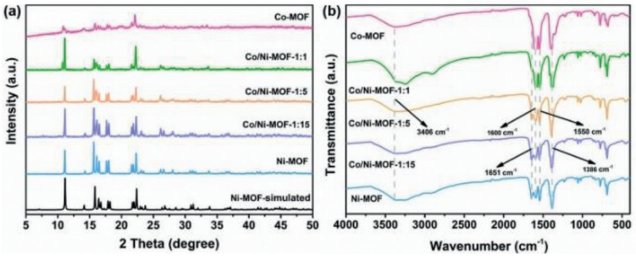

Fig. 2. (a) PXRD patterns of the simulated Ni-MOF ($Ni(4\text{-}Pyc)_2$), the as-synthesized Ni-MOF, Co/Ni-MOF-x:y and Co-MOF. (b) FT-IR spectra of the as-synthesized Ni-MOF, Co/Ni-MOF-x:y and Co-MOF.

simulated $M(4\text{-}Pyc)_2$ (M = Ni or Co) structure [28–30], confirming that the MOFs were successfully synthesized with high phase purity. The MOFs feature square lattice coordination networks assembled by linking six-coordinated M ions by 4-Pyc ligands (Fig. 1b). Each metal ion is six-coordinated by two pyridyl units and two bidentate carboxylate groups (Fig. S1 in Supporting information). The MOFs are composed of square shaped channels (7×7 Å) (Fig. 1b), which is large enough for electrolyte diffusion and storage, fast ion intercalation and deintercalation [23]. Fourier-transform infrared (FTIR) analyses of the series of MOFs are illustrated in Fig. 2b. Similar characteristic peaks are observed for all the materials, indicating that they possess identical functional groups. The peak at 3406 cm^{-1} is indexed to the stretching vibration of –OH [31]. The peaks located at ~1651 and ~1386 cm^{-1} are corresponding to the asymmetric and symmetric stretching vibrations of –COOH, respectively [31]. The peaks at ~1600 and ~1550 cm^{-1} are consistent with the stretching and bending vibration of pyridine ring [21,32].

The morphologies and microstructures of the synthesized MOFs are further investigated by scanning electron microscopy (SEM) and transmission electron microscopy (TEM). The SEM and TEM images show that the MOFs feature spindle-shaped micro/nanostructures (0.8–2.0 μm in length, 100–400 nm in diameter) with smooth surface (Figs. 3a1–e2) and solid nature (Figs. 3a3–e3). It is noteworthy that the introduction of Co ions has little effect on the structures and morphology of the MOFs that may be because the Co ion is similar in size to the original Ni ion. With the increase of the introduced Co ions, the sizes of the MOFs slightly decrease (Figs. 3b1 and b2) and then gradually increase (Figs. 3c1, c2, d1, d2, e1 and e2). The possible mechanism may be as follows. When a small amount of Co ions was introduced, the coordination ions is mainly Ni ions and the Co ions facilitate the coordination of Ni species, leading to fast nucleation and growth and affording smaller crystals. With the increasing amount of Co ions, the coordination competition of Co and Ni make the rate of nucleation and growth slow down, giving larger crystals [18,33]. Energy-dispersive X-ray (EDX) analysis shows the composition of Ni, Co, O, N and C in Co/Ni-MOF-1:15 (Fig. S2 in Supporting information). High-angle annular dark-field scanning TEM (HAADF-STEM) image and the corresponding elemental mappings demonstrate the homogeneous distribution of Ni, Co, O, N, and C elements (Figs. 3f–k), further verifying the successful preparation of Co/Ni-MOF-1:15. The mass ratios of $Ni^{2+}/(Co^{2+}+Ni^{2+})$ are 0.941, 0.904 and 0.572 in the Co/Ni-MOF-1:15, Co/Ni-MOF-1:5 and Co/Ni-MOF-1:1 from Inductively coupled plasma-atomic emission spectrometry (ICP-AES) elemental analysis (Table S1 in Supporting information), which is in consistent with the introduced initial feeding materials, suggesting the successful formation of the bimetallic MOFs. N_2 sorption measurement is performed to confirm the Brunauer-Emmett-Teller (BET) surface areas and the pore structures of Ni-MOF, Co/Ni-MOF-1:15 and Co-MOF. The Ni-MOF, Co/Ni-MOF-1:15 and Co-MOF exhibit the calculated BET surface areas of 212.1, 229.0 and 17.75 m^2/g with pore volumes of 0.1975, 0.2004 and 0.058 cm^3/g, respectively (Fig. S3 in Supporting information). The larger surface area and higher porosity of Co/Ni-MOF-1:15 allow faster electrolyte diffusion and ion transport. To be noted, the much smaller BET surface area and pore volume for Co-MOF is because its structure was completely collapsed under activation condition [30]. The thermal stability of Co/Ni-MOF-1:15 is investigated using thermogravimetric analysis (Fig. S4 in Supporting information). From room temperature to ~325 °C, the gradual weight loss is due to the loss of guest DMF molecules and the DMF molecules trapped inside the pores. As the temperature increases, the decomposition of the organic components occurs. In addition, no obvious phase change is observed when the Co/Ni-MOF-1:15 is immersed separately in water and ethanol solution for 24 h (Fig. S5 in Supporting information), demonstrating its favorable stability in these solutions.

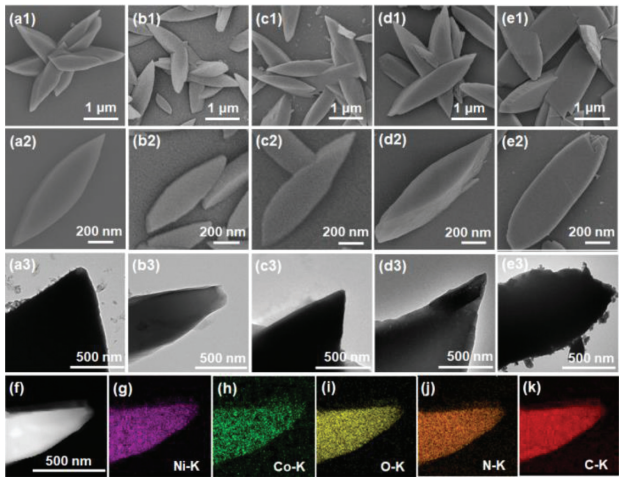

Fig. 3. (a1–e2) SEM images and (a3–e3) TEM images of Ni-MOF, Co/Ni-MOF-1:15, Co/Ni-MOF-1:5, Co/Ni-MOF-1:1, and Co-MOF. (f) HAADF-STEM image of Co/Ni-MOF-1:15 and (g–k) the corresponding elemental mapping of Ni–K, Co–K, O–K, N–K and C–K.

X-ray photoelectron spectroscopy (XPS) of the Ni-MOF, Co/Ni-MOF-1:15, Co/Ni-MOF-1:5, Co/Ni-MOF-1:1 and Co-MOF are performed to investigate their element composition and oxidation state on the surface. The survey spectrum confirms the presence of metal ions (Ni or Co/Ni or Co), O, N and C elements in the as-synthesized MOFs (Fig. 4a). In high-resolution Ni 2p spectrum of Ni-MOF, Co/Ni-MOF-1:15, Co/Ni-MOF-1:5 and Co/Ni-MOF-1:1 (Fig. 4b), two peaks with binding energies of 855.3 and 872.9 eV are assigned to Ni $2p_{3/2}$ and Ni $2p_{1/2}$, accompanied with two satellite peaks at 860.8 and 878.8 eV, respectively [34,35]. The characteristic binding energy of 17.6 eV verifies the presence of Ni^{2+} [36]. High-resolution Co 2p spectrum of Co/Ni-MOF-1:15, Co/Ni-MOF-

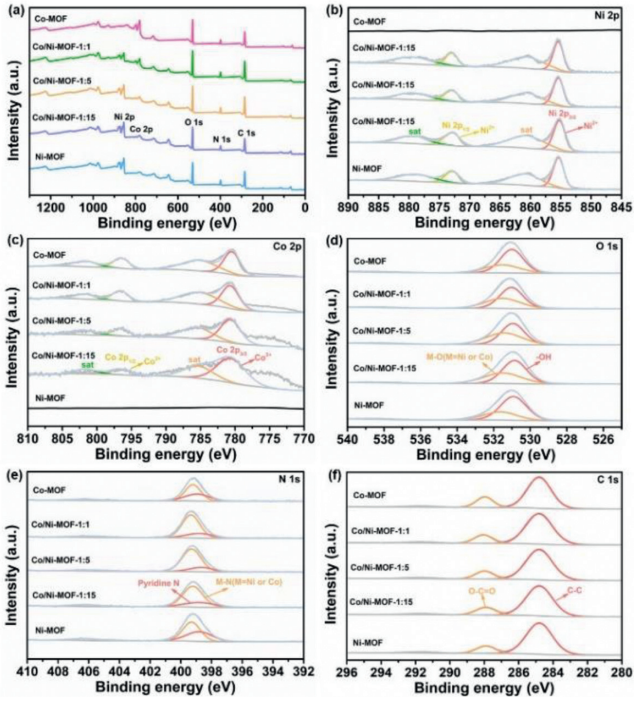

Fig. 4. XPS spectra for the Ni-MOF, Co/Ni-MOF-1:15, Co/Ni-MOF-1:5, Co/Ni-MOF-1:1 and Co-MOF. (a) Survey spectrum. (b) Ni 2p. (c) Co 2p. (d) O 1s. (e) N 1s. (f) C 1s.

1:5 Co/Ni-MOF-1:1 and Co-MOF can be divided into two spin-orbit peaks and two shake-up satellites (Fig. 4c). The peaks at 780.5 and 796.5 eV are indexed to Co $2p_{3/2}$ and Co $2p_{1/2}$ of Co^{2+} [37]. For the O 1s spectrum, two peaks at 530.8 and 531.5 eV are observed, which are attributed to the O in the –OH and M-O bonds, respectively (Fig. 4d) [38]. The N 1s spectrum can be deconvoluted into two peaks located at 398.8 and 399.2 eV, corresponding to the N in the pyridine N and M-N bonds, respectively (Fig. 4e) [39,40]. The peaks at 284.8 and 287.9 eV in the C 1s spectrum are assigned to the C−C and O−C=O, respectively (Fig. 4f) [41,42].

The electrochemical performance of the as-synthesized MOFs is investigated in a 3.0 mol/L KOH in a standard three-electrode system. The cyclic voltammetry (CV) curves of all the MOFs collected at a scan rate of 20 mV/s show well-defined redox peaks (Fig. 5a), corresponding to faradic pseudocapacitive behaviors. The redox behaviors can be assigned to Ni^{2+}/Ni^{3+} and/or Co^{2+}/Co^{3+} redox reactions occurred in the alkaline electrolyte [19,20]. In the CV curves of Co/Ni-MOFs, only one pair of redox peaks is observed that can be attributed to the overlapping of the closed redox peaks of Co and Ni [20]. A small amount of Co ions introduced to the Ni-MOF enables the enhancement of the properties of Ni species, thus the peak current of Co/Ni-MOF-1:15 and Co/Ni-MOF-1:5 is larger than that of Ni-MOF. As the amount of Co ions increases, the ratio of Ni ions relatively decreases, leading to the degrade of the peak current [33].

The CV curve of Co/Ni-MOF-1:15 shows the largest integral area and the highest current density, suggesting its highest specific capacitance. At the same time, the galvanostatic charge/discharge (GCD) curves exhibit that the discharge time of Co/Ni-MOF-1:15 at the current density of 0.5 A/g is the longest (Fig. 5b). The GCD profiles at different current densities from 0.5 A/g to 5 A/g are collected (Fig. S7 in Supporting information) and the specific capacitance are summarized in Fig. 5c. Co/Ni-MOF-1:15 exhibits the highest specific capacitance of 359 F/g at the current density of 0.5 A/g, which is superior to the Co/Ni-MOF-1:5 (293 F/g), Ni-

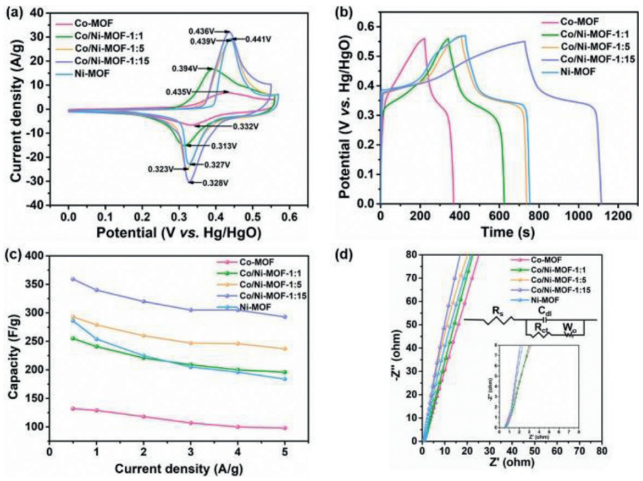

Fig. 5. Electrochemical performances of the Ni-MOF, Co/Ni-MOF-1:15, Co/Ni-MOF-1:5, Co/Ni-MOF-1:1 and Co-MOF. (a) CV curves at the scan rate of 20 mV/s. (b) GCD curves at a current density of 0.5 A/g. (c) Specific capacitances at different current densities. (d) EIS spectra.

MOF (286 F/g), Co/Ni-MOF-1:1 (255 F/g), and Co-MOF (132 F/g). With the increase of the current density, the specific capacitances for the MOFs are gradually decreased, and the Co/Ni-MOF-1:15 shows better rate performance than other samples, with the corresponding capacitance retention at 5 A/g is 81.5%. Electrochemical impedance spectroscopy (EIS) was characterized to investigate the charge-transfer kinetic resistance. The Nyquist plots (Fig. 5d) show that the semicircles in the high-frequency region for all the MOFs are not obvious, and the Co/Ni-MOF-1:15 presents the stepper straight line in the low-frequency region, indicating its small diffusion resistance, which allow faster ion diffusion of the electrolyte during the redox reaction. This result is in line with the CV and GCD curves. The long-term cycle performance of the Ni-MOF, Co/Ni-MOF-1:15 and Co-MOF was performed at 5 A/g. After 5000 cycles, 81% of the initial capacitance is retained, which is super to that of Ni-MOF (79%) and Co-MOF (51%) (Fig. S8 in Supporting information). The decrease of the capacitance is attributed to the collapse of the Co/Ni-MOF-1:15 (Fig. S9 in Supporting information), which may be caused by the repeated intercalation and deintercalation of OH^- at the interface of electrode/electrolyte during the cycling test [43].

The diffusive- and nondiffusive-controlled contributions were analyzed based on CV curves. The CV curves of Co/Ni-MOF-1:15 at the scan rates from 10 mV/s to 100 mV/s are presented in Fig. 6a. The well-defined oxidation/reduction peaks are originated from the redox reactions of Ni^{2+}/Ni^{3+} and/or Co^{2+}/Co^{3+}. The *b* values were 0.69/0.61 (Fig. 6b), suggesting the mixed charge storage of a diffusion-controlled process and a capacitive process. The CV curve of Co/Ni-MOF-1:15 at a scan rate of 10 mV/s shows that capacitive contribution is about 44.5% of the total capacitive (Fig. 6c). Fig. 6d shows the ratio of the contributions of the two processes. As the scan rate increases from 10 to 100 mV/s, the capacitive contributions are increased from 44.5% to 71.5%.

The excellent energy storage performance of Co/Ni-MOF-1:15 can be attributed to the following factors. (1) The square shaped channels (7×7 Å) are large enough for electrolyte diffusion and storage, fast ion intercalation and deintercalation (Fig. 1b); (2) The larger surface area and higher porosity of Co/Ni-MOF-1:15 allow faster electrolyte diffusion and ion transport (Fig. S3); (3) Co/Ni-MOF-1:15 exhibits lower diffusion resistance, facilitating ion diffusion of the electrolyte during the redox reaction (Fig. 5d); (4) The synergistic effect between the optimal ratio of Co^{2+} and Ni^{2+} in Co/Ni-MOF-1:15 facilitate to provide more active sites [21,33,44].

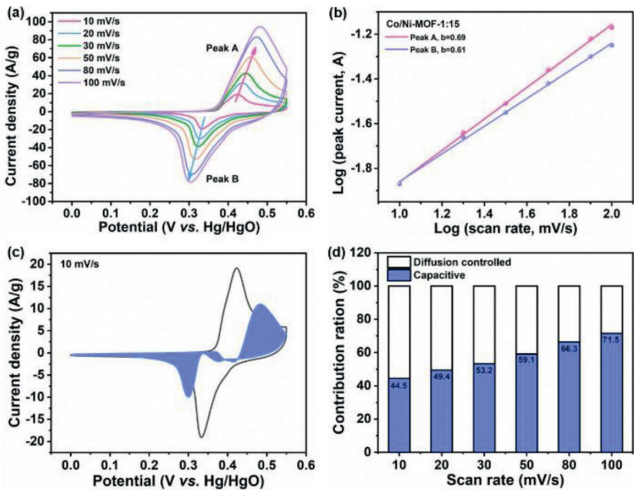

Fig. 6. (a) CV curves of the Co/Ni-MOF-1:15 at different scan rates. (b) The plot of log(*i*) *versus* log(*v*). (c) Separation of the diffusion and capacitive-controlled currents of Co/Ni-MOF-1:15 at 10 mV/s. (d) Relative contribution of the diffusion and capacitive-controlled charge storage at different scan rates.

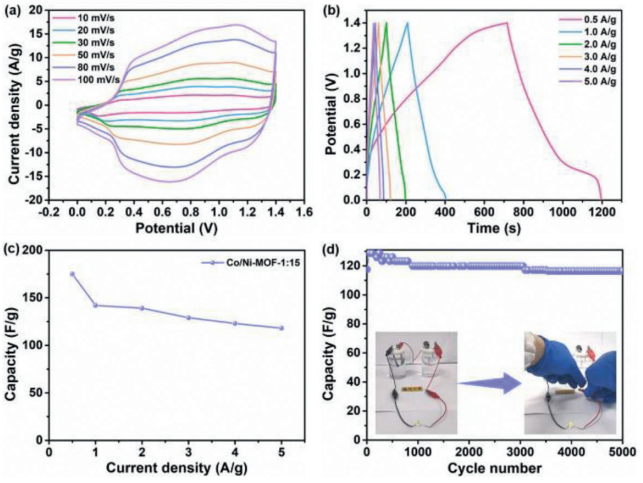

Fig. 7. Electrochemical performances of the Co/Ni-MOF-1:15//AC. (a) CV curves at different scan rates. (b) GCD curves at different current densities from 10 mV/s to 100 mV/s. (c) Specific capacitances at different current densities. (d) Cycling performance at 5 A/g (inset: schematic illustration of Co/Ni-MOF-1:15//AC to light a yellow light-emitting diode).

To further evaluate the feasibility of Co/Ni-MOF-1:15 at the device level, a two-electrode asymmetric device is constructed using Co/Ni-MOF-1:15 as the positive electrode and activated carbon (AC) as the negative electrode in a 3 mol/L KOH electrolyte (denoted as Co/Ni-MOF-1:15//AC). The CV curves of the Co/Ni-MOF-1:15//AC at different potential windows at a scan rate of 20 mV/s shows no obvious polarization, suggesting that a stable operating voltage window can be extended to 1.42 V (Fig. S18 in Supporting information). The CV curves of Co/Ni-MOF-1:15//AC at the scan rates from 10 mV/s to 100 mV/s show the *quasi*-rectangular shapes that can be attributed to the charge generating from the battery-type electrode and electrical double layer electrode (Fig. 7a). The GCD curves of Co/Ni-MOF-1:15//AC at different current densities from 0.5 A/g to 5 A/g are almost symmetric (Fig. 7b), revealing its excellent electrochemical reversibility. The calculated specific capacitance is 175, 142, 139, 128.6, 122.8, 121.4 F/g at the current densities of 0.5, 1, 2, 3, 4, 5 A/g, respectively (Fig. 7c). Moreover, excellent cycle performance with 97.1% capacity retention after 5000 cycles was achieved for Co/Ni-MOF-1:15//AC when investigated at the current density of 5 A/g (Fig. 7d), which is better than NiCo-MOF-1 [45] and NiCo-$MOF_{0.75}$ [46], and is comparable to CoNi23/CFP [33], MXene@Ni-MOF [47] and COP [48]. Notably, the specific capacitance shows a growth at the beginning cycles, which may be due to the activation of the electrode materials and the gradual permeation of the electrode through the electrode [49,50]. Furthermore, the Co/Ni-MOF-1:15//AC device can light up a yellow light-emitting diode (operating voltage 1.6–3 V, 20 mA), demonstrating its potential for practical applications.

In summary, a series of spindle-like metal-organic micro/nanostructures have been fabricated by solvothermal synthesis. Benefitting from the structural merits and the synergistic effect between the optimum ratio of Co^{2+} and Ni^{2+}, the Co/Ni-MOF-1:15 shows a high specific capacitance of 359 F/g at 0.5 A/g with good rate performance and cycling stability as an electrode for supercapacitor. The Co/Ni-MOF-1:15//AC ASC electrode achieves a specific capacitance of 175 F/g at the current density of 0.5 A/g excellent cycling performance with 97.1% retention after 5000 cycles at 5 A/g. This work demonstrates that the fabrication of bimetallic-organic micro/nanostructures is an effective strategy to enhance the specific capacitance, rate performance and cyclability.

Declaration of competing interest

The authors declare that they have no known competing financial interests or personal relationships that could have appeared to influence the work reported in this paper.

Acknowledgments

This work was supported by the National Natural Science Foundation of China (NSFC, Nos. 21901222, U1904215 and 21671170), Lvyangjinfeng Talent Program of Yangzhou, Top-notch Academic Programs Project of Jiangsu Higher Education Institutions (TAPP), Program for Young Chang Jiang Scholars of the Ministry of Education, China (No. Q2018270), and Natural Science Foundation of Jiangsu Province (No. BK20200044).

Supplementary materials

Supplementary material associated with this article can be found, in the online version, at doi:10.1016/j.cclet.2022.107787.

References

[1] H.L. Li, M. Eddaoudi, M. O'Keeffe, O.M. Yaghi, Nature 402 (1999) 276–279.
[2] H.C. Zhou, J.R. Long, O.M. Yaghi, Chem. Rev. 112 (2012) 673–674.
[3] H. Furukawa, K.E. Cordova, M. O'Keeffe, O.M. Yaghi, Science 341 (2013) 1230444.
[4] L.L. Zou, C.C. Hou, Z. Liu, H. Pang, Q. Xu, J. Am. Chem. Soc. 140 (2018) 15393–15401.
[5] Y.H. Wen, J. Zhang, Q. Xu, X.T. Wu, Q.L. Zhu, Coord. Chem. Rev. 376 (2018) 248–276.
[6] Z. Jiang, X.H. Xu, Y.H. Ma, et al., Nature 586 (2020) 549–554.
[7] B. Liang, X. Zhang, Y. Xie, et al., J. Am. Chem. Soc. 142 (2020) 17795–17801.
[8] Y.Y. Xue, X.Y. Bai, J. Zhang, et al., Angew. Chem. Int. Ed. 60 (2021) 10122–10128.
[9] Z.H. Zhu, Y.B. Liu, C. Song, et al., ACS Nano 16 (2022) 1346–1357.
[10] D. Sheberla, J.C. Bachman, J.S. Elias, et al., Nat. Mater. 16 (2017) 220–224.
[11] S.S. Zheng, Q. Li, H.G. Xue, H. Pang, Q. Xu, Natl. Sci. Rev. 7 (2020) 305–314.
[12] D.W. Feng, T. Lei, M.R. Lukatskaya, et al., Nat. Energy 3 (2018) 30–36.
[13] X. Xiao, L.L. Zou, H. Pang, Q. Xu, Chem. Soc. Rev. 49 (2020) 301–331.
[14] X.X. Hang, Y.D. Xue, M. Du, et al., Inorg. Chem. Front. 9 (2022) 2845–2851.
[15] S.S. Zheng, Y. Sun, H.G. Xue, et al., Natl. Sci. Rev. 9 (2022) nwab197.
[16] G.X. Zhang, L. Jin, R.X. Zhang, et al., Coord. Chem. Rev. 439 (2021) 213915.
[17] Y.X. Xu, Q. Li, H.G. Xue, H. Pang, Coord. Chem. Rev. 376 (2018) 292–318.
[18] N. Raza, T. Kumar, V. Singh, K.H. Kim, Coord. Chem. Rev. 430 (2021) 213660.
[19] D. Tian, N. Song, M.X. Zhong, X.F. Lu, C. Wang, ACS Appl. Mater. Interfaces 12 (2020) 1280–1291.
[20] S.W. Gao, Y.W. Sui, F.X. Wei, et al., J. Colloid Interface Sci. 531 (2018) 83–90.
[21] X.X. Hang, Y.D. Xue, Y. Cheng, et al., Inorg. Chem. 60 (2021) 13168–13176.
[22] J. Yang, C. Zheng, P.X. Xiong, Y.F. Li, M.D. Wei, J. Mater. Chem. A 2 (2014) 19005–19010.
[23] Y. Jiao, J. Pei, D.H. Chen, et al., J. Mater. Chem. A 5 (2017) 1094–1102.

[24] W.H. Li, K. Ding, H.R. Tian, et al., Adv. Funct. Mater. 27 (2017) 1702067.
[25] S.S. Zheng, Y. Ru, H.G. Xue, H. Pang, Chin. Chem. Lett. 32 (2021) 3817–3820.
[26] C.H. Wang, D.W. Zhang, S. Liu, et al., Chem. Commun. 58 (2022) 1009–1012.
[27] L. Kang, S.X. Sun, L.B. Kong, J.W. Lang, Y.C. Luo, Chin. Chem. Lett. 25 (2014) 957–961.
[28] S. Nandi, S. Collins, D. Chakraborty, et al., J. Am. Chem. Soc. 139 (2017) 1734–1737.
[29] M. Kang, S. Yoon, S. Ga, et al., Adv. Sci. 8 (2021) 2–8.
[30] M. Kang, D.W. Kang, J.H. Choe, et al., Chem. Mater. 33 (2021) 6193–6199.
[31] J.M. Zheng, J. Tian, D.X. Wu, et al., Nano Lett. 14 (2014) 2345–2352.
[32] Y. Bai, G.X. Zhang, S.S. Zheng, et al., Sci. China Mater. 64 (2021) 137–148.
[33] X.Y. Chu, F.L. Meng, T. Deng, et al., Nanoscale 12 (2020) 5669–5677.
[34] H. Mei, Y.J. Mei, S.Y. Zhang, et al., Inorg. Chem. 57 (2018) 10953–10960.
[35] G. Nagaraju, G.S.R. Raju, Y.H. Ko, J.S. Yu, Nanoscale 8 (2016) 812–825.
[36] J. Yang, P.X. Xiong, C. Zheng, H.Y. Qiu, M.D. Wei, J. Mater. Chem. A 2 (2014) 16640–16644.
[37] Z.L. Zhao, H.X. Wu, H.L. He, X.L. Xu, Y.D. Jin, Adv. Funct. Mater. 24 (2014) 4698–4705.
[38] L. Yang, G.L. Zhu, H. Wen, et al., J. Mater. Chem. A 7 (2019) 8771–8776.
[39] H.T. Liu, J.Y. Guan, S.X. Yang, et al., Adv. Mater. 32 (2020) 1–8.
[40] Z.H. Zou, J.L. Wang, H.R. Pan, et al., J. Mater. Chem. A 8 (2020) 14099–14105.
[41] L.L. Zou, C.C. Hou, Q.J. Wang, et al., Angew. Chem. Int. Ed. 59 (2020) 19627–19632.
[42] F.Z. Sun, G. Wang, Y.Q. Ding, et al., Adv. Energy Mater. 8 (2018) 1–11.
[43] Y. Li, Y.X. Xu, Y. Liu, H. Pang, Small 15 (2019) 1–8.
[44] J. Wang, Q. Zhong, Y.Q. Zeng, et al., J. Colloid Interface Sci. 555 (2019) 42–52.
[45] Y. Chi, W.P. Yang, Y.C. Xing, et al., Nanoscale 12 (2020) 10685–10692.
[46] X.L. Zhang, J.M. Wang, X. Ji, et al., J. Alloy. Compd. 825 (2020) 154069.
[47] S.S. Zheng, H.J. Zhou, H.G. Xue, P. Braunstein, H. Pang, J. Colloid Interface Sci. 614 (2022) 130–137.
[48] Q.L. Jing, W.T. Li, J.J. Wang, X.D. Chen, H. Pang, Inorg. Chem. Front. 8 (2021) 4222–4229.
[49] W.Q. Ye, P.C. Ye, H.Y. Wang, et al., J. Colloid Interface Sci. 612 (2022) 298–307.
[50] W. Lu, J.L. Shen, P. Zhang, et al., Angew. Chem. Int. Ed. 58 (2019) 15441–15447.